Dalton Transactions

PAPER

View Article Online
View Journal | View Issue

Cite this: *Dalton Trans.*, 2019, **48**, 10915

Iron(II) complexes with diazinyl-NHC ligands: impact of π-deficiency of the azine core on photophysical properties†

Mohamed Darari,[a] Edoardo Domenichini,[b] Antonio Francés-Monerris,[c] Cristina Cebrián,[d] Kevin Magra,[d] Marc Beley,[a] Mariachiara Pastore,[c] Antonio Monari,[c] Xavier Assfeld,[c] Stefan Haacke[b] and Philippe C. Gros*[a]

Ligand field enhancing N-heterocyclic carbene (NHC) ligands were recently shown to prevent photo-induced spin crossover in Fe(II) complexes due to their intricate effects on the electronic excited state structure. Due to their pico- to nanosecond lifetimes, these complexes are now good candidates for photo-sensitizing applications. Herein we report the synthesis and photophysical characterization of a new family of homoleptic Fe(II) complexes with C^N^C ligands involving diazines as the central N-heteroaromatic ligand. For these four carbene bond complexes, ultrafast transient absorption spectroscopy revealed a significant improvement of the excited-state lifetime. A record 32 ps lifetime was measured for a complex bearing a ligand combining a π-deficient pyrazine nucleus and a benzimidazolylidene as NHC. When compared to other azine-based ligands investigated, we argue that the lifetimes are modulated by a small excited state barrier expressing the ability of the ligand to reach the Fe–N distance needed for internal conversion to the ground state.

Received 25th April 2019,
Accepted 24th May 2019

DOI: 10.1039/c9dt01731c

rsc.li/dalton

Introduction

Photoactive metal complexes play a pivotal role in several excitonic devices.[1–3] Such applications require the smart design of ligands to finely control the optical and electrochemical properties of the metal complexes. Due to their optimal photophysical features, noble metals, such as ruthenium or platinum, allow the design and fabrication of devices having impressive properties in terms of efficiency or tenability.[4,5] However, such success comes with a price to pay; notably the low abundance, relatively high cost and toxicity of such metals, that may strongly limit their employment in larger scale industrial productions. Thus, finding alternative routes, by using less toxic and more abundant metals such as iron, would highly reduce the cost and the environmental impact of man-made technology. However, the fine control of the photophysical behaviour of first-row transition metal complexes is particularly challenging. Indeed, and as a most significant example, while the excited state evolution of ruthenium(II) polypyridyl complexes is dominated by long-lived metal-to-ligand (MLCT) triplet states,[6] a sub picosecond relaxation to metal centred (MC) states followed by an ultrafast ground-state recovery is observed for the iron analogues.[7–10] Most notably, this ultrafast non-radiative deactivation is the main reason precluding the successful utilization of iron complexes in photochemical applications requiring stabilized MLCT states, such as dye sensitized solar cells (DSSCs),[5] or in emissive devices.

Recently, several groups have raised the challenge and proposed the design of photoactive iron complexes by increasing the ligand field splitting with the aim to destabilize the metal centred states.[11] In this context, a considerable breakthrough has been achieved using pyridyl N-heterocyclic carbenes (NHC) as ligands combining the π-deficiency of pyridine and the σ-donating property of NHC.[12,13] Indeed, excited-state lifetimes of tens and hundreds[14] of picoseconds, have been obtained for iron(II) complexes with tridentate[15,16] and bidentate[17,18] pyridyl-NHC ligands.

The influence of the conjugation pattern and peripheral substituents on the electronic properties of NHC has also been investigated by switching from imidazolylidene to benzimidazolylidene (BIm) or modifying the alkyl chain showing a notable improvement of the MLCT lifetime.[15] In contrast, the effect of the nature of the central azine core has not been investigated yet, while the increase of its π-deficiency might be a promising route to promote an additional stabilization of the

[a]*Université de Lorraine, CNRS, L2CM, F-54000 Nancy, France. E-mail: philippe.gros@univ-lorraine.fr*
[b]*Université de Strasbourg, CNRS, IPCMS, F-67000 Strasbourg, France*
[c]*Université de Lorraine, CNRS, LPCT, F-54000 Nancy, France*
[d]*Université de Lorraine, CNRS, L2CM, F-57000 Metz, France*

† Electronic supplementary information (ESI) available: See DOI: 10.1039/c9dt01731c

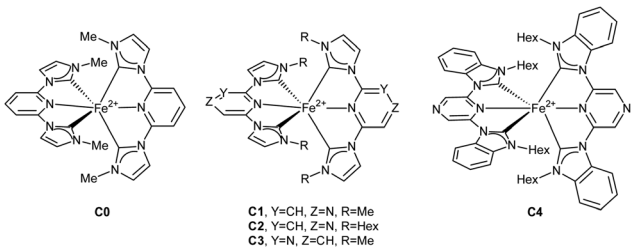

Fig. 1 Complexes studied in this work. In all cases, counter ion is PF_6^- in any case.

MLCT states when combined with the NHC-induced destabilization of the MC states.

In this contribution we report the synthesis of new diazinyl-NHC ligand precursors **L1–L5** containing π-deficient pyrazine and pyrimidine and their corresponding iron(II) complexes **C1–C4** (Fig. 1). The excited-states decay of the organometallic complexes was characterized by ultrafast time-resolved spectroscopy and by modelling the potential energy surfaces (PESs) *via* time-dependent density functional theory (TD-DFT).

Results and discussion

Synthesis

The ligand precursors **L1–L5** required for the preparation of the target complexes have been obtained in good yields from both dichloro pyrazine and pyrimidine according to Scheme 1. The ligands have been designed bearing short and long alkyl chains and different counter-anions to anticipate solubility concerns as well as anion effects along the coordination process with iron(II).[19,20]

The coordination of the new ligands with iron(II) to obtain the complexes **C1–C4** is performed as reported in Scheme 2. The ligands **L1**, **L2** and **L3** were reacted with a mixture of $FeBr_2$ and hexamethyldisilazide (KHMDS) leading to the target complexes **C1**, **C2** and **C3** respectively. The process used above was not effective for the synthesis of **C4**. In this case, the carbene was first generated by initial deprotonation of **L5**. Br by LiHMDS followed by reaction with $FeBr_2$. In this case, due to solubility issues, only the ligands bearing the hexyl chain led to the expected complex **C4**.

Electronic and electrochemical properties

The electronic properties of the complexes **C1–C4** were preliminary investigated by means of steady-state UV-vis spectroscopy (Fig. 2) and cyclic voltammetry (Table 1). The data related to complex **C0** have been also included for the sake of comparison.

For all the complexes, the absorption spectra are composed of three bands. Intense band in the UV region and below 350 nm (not shown here) corresponds to π–π* transitions centred on the ligands, and as expected, they are much more intense for **C4** bearing the four BIm moieties.

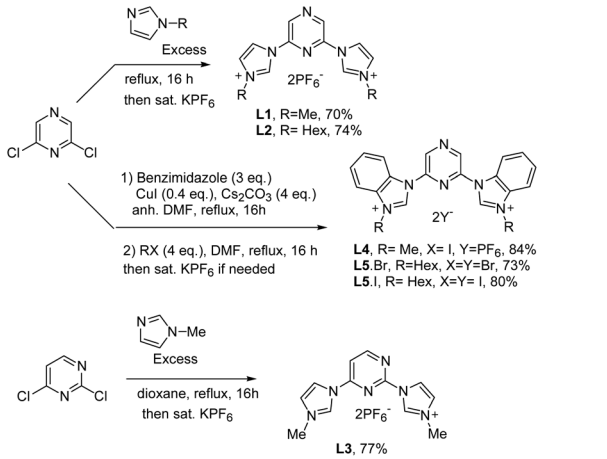

Scheme 1 Synthesis of ligands **L1–L5**.

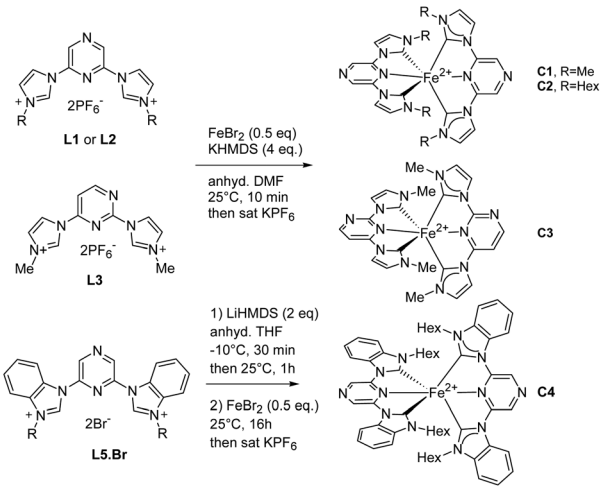

Scheme 2 Synthesis of complexes **C1–C4**.

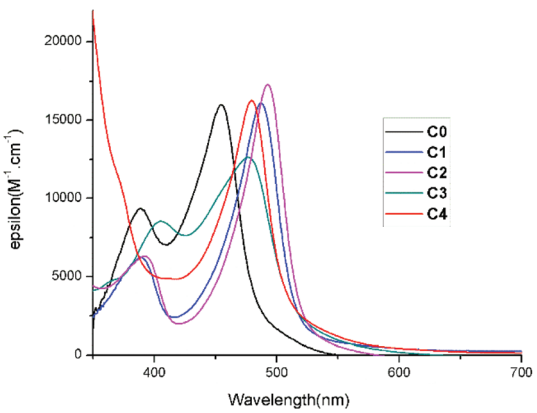

Fig. 2 UV-Vis spectra of **C0–C4** in acetonitrile. The portion of the spectrum below 350 nm is not shown due to intense UV bands in case of **C4**.

Table 1 Photophysical and electrochemical properties of complexes

	$\lambda_{abs\text{-}max}$ [a] (nm) (ε (M^{-1} cm^{-1}))	E_{ox} (Fe^{III}/Fe^{II})[b] (V/SCE)	E_{red1} (V/SCE)	ΔE[c] (eV)
C0	393 (9000) 460 (15 900)	0.80 (rev)	−1.95 (irrev.)	2.75
C1	389 (6300) 487 (16 100)	0.98 (rev)	−1.39 (rev)	2.37
C2	392 (6200) 493 (17 300)	1.09 (rev)	−1.32 (rev)	2.41
C3	406 (8500) 477 (12 600)	0.93 (rev)	−1.70 (irrev)	2.63
C4	350 (sh)(11 000) 479 (16 200)	1.22 (rev)	−1.21 (rev)	2.43

[a] Measured in CH_3CN at 25 °C. [b] First oxidation potential. Potentials are quoted *vs* SCE. Under these conditions, $E_{1/2\ (Fc+/Fc)} = 0.39\ V^{-1}$ S.C.E. Recorded in CH_3CN using $Bu_4N^+PF_6^-$ (0.1 M) as supporting electrolyte at 100 mV s^{-1}. [c] Electrochemical band gap ($\Delta E = E_{ox} - E_{red1}$).

At longer wavelengths, all the complexes exhibit two distinct bands associated to MLCT transitions and presenting significant shifts and changes in the band-shape as a function of the ligands. The bands in the 360–420 nm range are related to carbene-Fe MLCT transitions[15,21] while the bands in the 430–600 nm area are due to the azine-Fe MLCTs. As a general trend, a notable red-shift of 30–40 nm of the azine-Fe band as compared to **C0** was observed for all the new complexes. This observation is in full agreement with the increased π-deficiency of the central azine when switching from pyridine to pyrazine and pyrimidine. Furthermore, BIm promotes a blue shift of both azine-Fe and carbene-Fe transitions, as can be noticed by comparing the absorption spectra of **C1** and **C4**, as a result of an increased π-back donation from the metal, thus stabilizing the occupied iron t_{2g} orbitals and as a consequence the ground state.[15] While the carbene-Fe transition was not affected when going from pyridine to pyrazine (compare **C0**, **C1** and **C2**), the use of pyrimidine as the central azine induced a non-negligible red-shift of 30 nm, and a general broadening of the 430–600 nm band, with the appearance of a broader shoulder around 450 nm. This may be due to the reduced point group symmetry of **C3** as compared to the other complexes.

Fig. S17† shows the TD-DFT spectra of **C1**, **C2**, **C3** and **C4**. Even though the lowest-energy bands are blue shifted by around 0.3 eV with respect to the experimental results, the trends described above are correctly reproduced by the computational protocol. The analysis of the natural transition orbitals (NTOs)[22] further confirms the MLCT nature of the excitations involving the lowest-energy bands (see Fig. S18–20†) and their assignment, whereas some contributions of inter-ligand (IL) states are predicted for the intense band of **C4** appearing at higher energies (see Fig. S20†).

The electrochemical profiles (Table 1) globally confirm the trends underlined by the absorption spectroscopy studies. Due to their higher π-deficiencies, pyrazine and pyrimidine promoted an increase of the Fe^{II}/Fe^{III} oxidation potential as compared to **C0**, an effect that is even higher for **C4** due to the electron-accepting effect of BIm.

The reduction potentials were also strongly affected and generally increased going from **C0** to **C4**. Since reduction reflects the injection of one electron into the antibonding π* orbitals these results can, in a first approximation, be rationalized as a more efficient stabilization of the LUMO orbital by pyrazine than pyridine. However, **C3** represents an exception to the trend, indeed the reduction potential was less significantly modified with respect to the other complexes.

Ultrafast transient absorption spectroscopy

In order to get further insights into the impact of the new ligands on the photophysical properties, the four complexes were investigated by femtosecond transient absorption spectroscopy (TAS) at room temperature. All samples are dissolved in CH_3CN and excited at 480 nm.

For **C4**, Fig. 3A, three signals are observed, two positive bands (excited state absorption ESA) and one negative (ground state bleach GSB). Between such signals, two isosbestic points are identified at 428 and 500 nm. The dot-dashed line corresponds to the inverse of the normalised steady-state absorption (SSA) scaled on the TA spectra at 484 nm, the maximum of GSB. This spectrum has a perfect overlap with the TA-spectra in the range 440–491 nm, while outside, the ESA signals are significantly adding up to the GSB, which implies a decrease of the GSB intensity. The positive bands have a different trend,

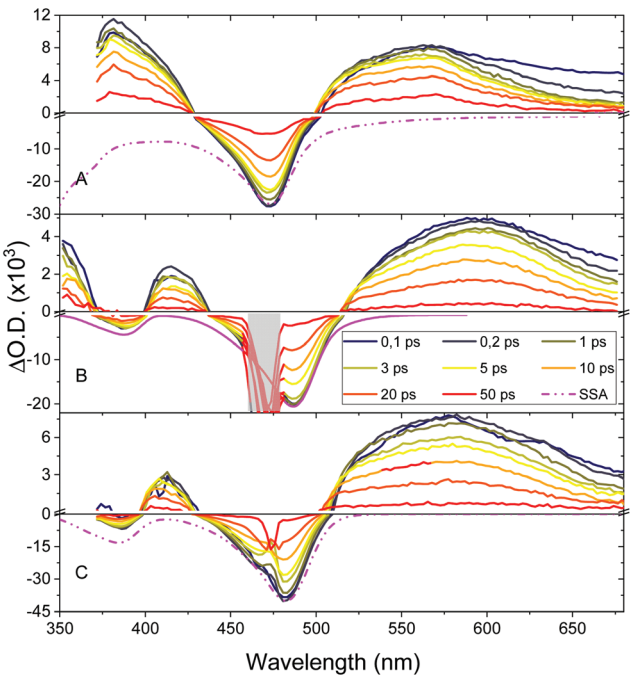

Fig. 3 Selected transient absorption spectra of **C4** (A), **C2** (B), **C1** (C) in AcN excited at 480 nm. Delay times are from 0.1 ps (blue) to 50 ps (red). Spectra of C4 and C2 display mainly intensity/exc. state population decay, while the spectra of C1 are subject to shifts and changes in shape until ≈20 ps. Inverted steady state absorption (SSA) spectra are shown for comparison (dot-dashed pink line). Note different scale for positive and negative parts of *y*-axes. In B, grey shaded area denotes excessive pump beam scatter.

indeed the blue one (λ < 428 nm) does not present any time-evolution, in contrast to the redder one (λ > 500 nm), which can be split into two ranges: 500–590 nm where the intensity purely decays (shape conserved in time) while in the range 590–690 nm the spectra evolve within ≈1 ps before reaching a stable shape. This trend is highlighted in the spectra normalised at 473 nm (Fig. SI23†).

All the spectra at t > 1 ps overlay over the full wavelength range regions, while, at earlier times, a slight spectral evolution is visible.

In Fig. 3B, selected spectra of **C2** are shown. In variance with C4, two negative bands (GSB) are observed, peaking at 388 and 487 nm, and three positives (ESA) at λ < 370 nm, 410 and 578 nm. Four isosbestic points are identified at 370, 400, 435 and 516 nm. The SSA, normalized at 487 nm, overlaps perfectly in the red side of the main GSB (λ > 487 nm) while, in the blue part (λ < 487 nm), the intensity is ≈30% lower than the SSA. This small discrepancy, also in this case, points to an overlapping ESA at these wavelengths. The shape of the long-wavelength ESA presents a small evolution in time, which is better seen in Fig. SI25,† where the normalized spectra show for the long-wavelength ESA, at λ > 525 nm narrowing, and a small dynamic shift. This causes the isosbestic point at 516 nm to shift by ≈5 nm in the first 20 ps.

The kinetics of **C4**, at relevant wavelengths, are plotted in a semi-log scale and reported in Fig. 4. They are normalised and multiplied by an arbitrary factor. The dashed lines highlight the mono-exponential decay associated with a lifetime of ~30 ps. The kinetic traces are well approximated, on this time scale, by the mono-exponential decay, but some present small deviations *i.e.* additional short decay components at t < 5 ps with small amplitudes.

For **C2**, the kinetics are processed as before and plotted in Fig. SI27.† Most of the kinetics appear to be mono exponential, but for a precise analysis three lifetimes are necessary (see below). For **C4** and **C2**, the minor dynamic shifts of the TA spectra are compatible with the use of a global fit approach.[23] The obtained DAS are reported in Fig. 5. For **C4** (panel A), the analysis converges to τ_1 = 90 fs, τ_2 = 2 ± 1 ps and τ_3 = 33 ± 2 ps whereas for **C2** the fitting yields τ_1 = 100 fs, τ_2 = 4 ± 1 and τ_3 = 23 ± 2 ps. In both samples, the DAS associated with τ_1 indicate contributions both from an almost unresolved ESA relaxation and the solvent response (limited to the instrument response function), while the amplitude and shape of the 2 and 4 ps DAS are consistent with the minor spectral evolutions on this time scale.

In analogy to previous work,[15,24] the decay times are interpreted along the reaction scheme (1).

$$^1\mathrm{MLCT}^+ \xrightarrow{<\mathrm{IRF}} {}^1\mathrm{MLCT} \xrightarrow{\tau_1} {}^3\mathrm{MCLT}/{}^3\mathrm{MC}_{\mathrm{hot}} \xrightarrow{\tau_2} ({}^3\mathrm{MCLT}/{}^3\mathrm{MC})_{\mathrm{eq}} \xrightarrow{\tau_3} S_0 \quad (1)$$

Intersystem crossing (IC) occurs on the ≈0.1 ps time scale,[7–10] leading to a non-emissive triplet species (no stimulated emission). It can be associated with a non-equilibrated state of MLCT, MC or mixed character (see computational part below,[17] which decays within τ_2 into the vibrationally equili-

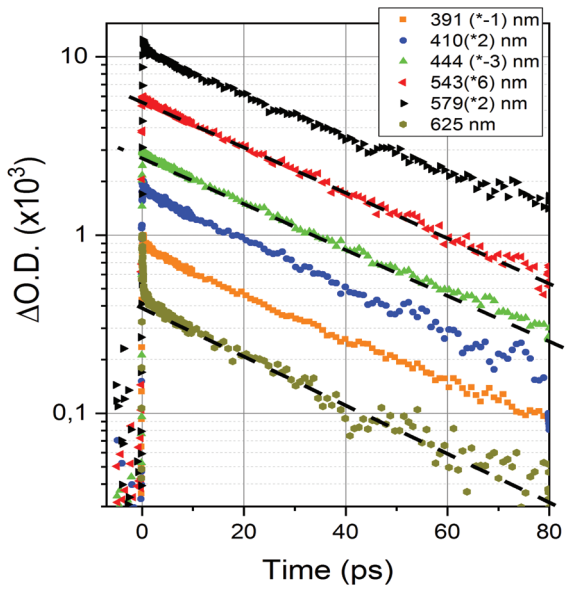

Fig. 4 Selected kinetics of **C4** plotted in semi-log scale. The kinetics are normalised and multiplied for an arbitrary factor as reported in the legend. For the GSB a negative factor is used. Dashed lines lines indicate the ~30 ps decay. Small deviations from the single exponential behaviour at early times relate to the minor spectral evolutions discussed in the text.

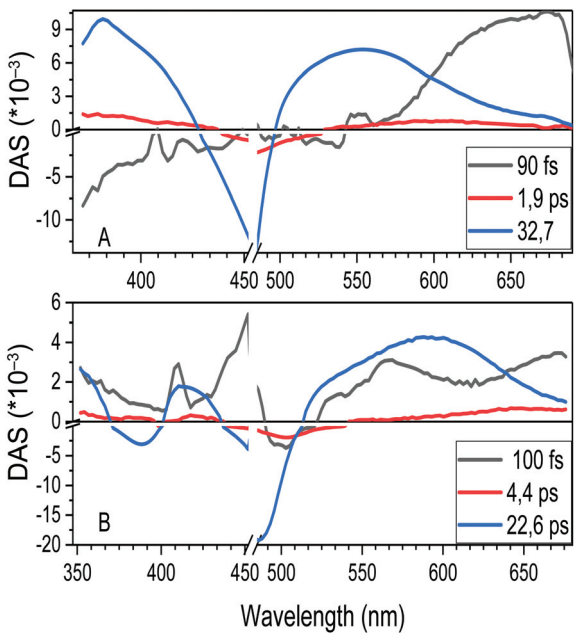

Fig. 5 Decay-associated difference spectra of C4 (A) and C2 (B) obtained with Glotaran (see ref. 22). The DAS associated with τ_1 have contributions from ESA and solvent response. The amplitude and shape of the 1.9 and 4.4 ps DAS are consistent with the minor spectral evolutions on this time scale.

Table 2 Time constants derived from the analysis of the TAS data[a]

Complex	τ_1 (ps)	τ_2 (ps)	τ_3 (ps)
C1	0.10 ± 0.05	2–6	21–25
C2	0.10 ± 0.05	4 ± 1	22 ± 2
C3	0.10 ± 0.05	2–4	11–12
C4	0.10 ± 0.05	1.5 ± 0.5	32 ± 3

[a] τ_3 is the excited state lifetime, and τ_1 and τ_2 describe excited state relaxation according to the sequential reaction scheme (see below). In the absence of global fitting, ranges of values are indicated for **C1** and **C3**.

brated $(^3MLCT/^3MC)_{eq}$. This relaxation step is manifested by the small spectral shifts (Fig. 3), which were not analysed in previous work.[24,25] After this relaxation step, related to structural or solvent relaxation, the population lives 32 ps for **C4** and 22 ps for **C2** (Table 2).

Pronounced spectral shifts in compounds C1 and C3

Unlike the previous cases, the data for complexes **C1** and **C3** show pronounced dynamic shifts and narrowing of the ESA. This is highlighted in Fig. 3C for **C1**, which has the same chemical structure as **C2**, except that the Hex chains are replaced by methyl groups (*cf.* Scheme 2). **C1** and **C2** have a very similar excited state decay times (τ_3 = 21–22 ps, Table 2), but obvious differences in their ESA spectra (Fig. 3B and C). Not only are the ESA transition energies slightly higher for **C1**, the spectra display pronounced dynamic shifts (no isosbestic point) and narrowing of the long-wavelength ESA band, indicative of a more significant excited state relaxation on time scales >3 ps. This is best highlighted by the normalised data (Fig. SI28†). The data for **C3** display even stronger relaxation effects, and a shorter τ_3 lifetime (11–12 ps), as summarized in the ESI.†

For **C1**, the modifications of the ESA spectrum in the initial 0.1–0.2 ps are due to ultrafast IC as above. For delays until ≈10 ps, the ESA decays faster on the long wavelength side (≥530 nm), flattens and shifts to shorter wavelengths. This gives rise to a decay at λ > 530 nm, and a rise component in the 490–520 nm range (*cf.* Fig. 6).

The result is the progressively shifting ESA/GSB crossover point around 500–510 nm. A similar decay/blue-shift behaviour is also observed in the minor ESA band at 410–430 nm. The ESA difference spectra steepen progressively in the 500–525 nm range (Fig. SI28†). Even though the effect may appear small, global fitting cannot be used any longer since the ESA extinction coefficient is time dependent $\varepsilon(\lambda,t)$, *i.e.* the often-made assumption of separability of wavelength and time dependencies does not hold. Note that in the present case, spectral evolution and excited state decay occur on similar time scales, particularly for **C3** (Table 2).

The results of 20 three-component fits performed for individual wavelengths are given in Fig. 7. The wavelength-dependent lifetimes are highlighted in the top panel, especially for τ_2 and τ_3. The latter represents the excited state lifetime of **C1**,

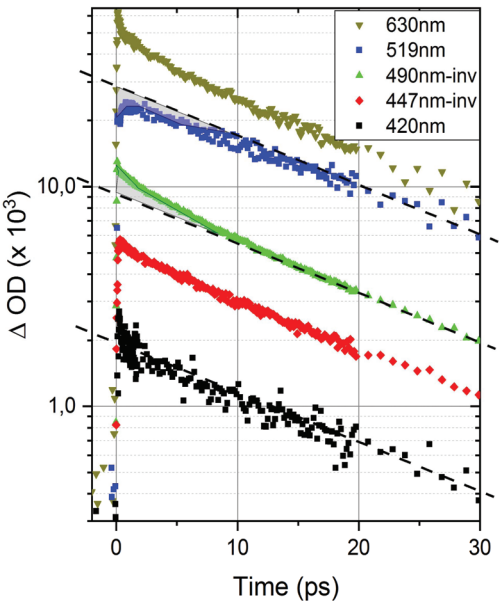

Fig. 6 Kinetic traces of TAS for **C1**, on a semi-log scale. The selected wavelengths cover the minor ESA band (420 nm), the main GSB (447 and 490 nm) and ESA (519 and 630 nm). The GSB traces are shown with inverted signs, and all traces except for 420 nm are shifted on the log scale by arbitrary factors. Dashed lines represent a ≈20 ps decay time, as guides-to-the-eye. Shaded areas in the 490 and 519 nm traces highlight the deviations from single exponential decay for t < 10 ps. For these wavelengths, they are due to the dynamic shift of the ESA spectrum, also seen at 630 nm, on a 2–6 ps time scale. These effects are smaller for the minor ESA band (<450 nm).

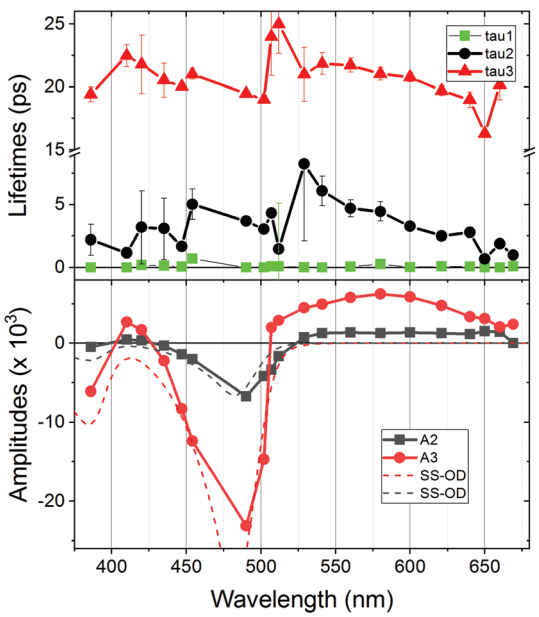

Fig. 7 Results of 3-component fits for **C1**. Top: Lifetimes in ps; bottom: amplitudes of the relevant components τ_2 and τ_3. Dashed lines show the scaled and inverted steady-state absorption spectra (SS-OD). Data in the range 460–480 nm are not analysed due to pump laser scatter. The decay-associated amplitudes (bottom) follow approximately the shape of GSB and ESA (Fig. 3), *i.e.* they are mostly associated with their decay times; except for the 490–530 nm region, where A_2 represents an ESA rise time.

characterised by the average ground state bleach recovery of 21 ± 1 ps in the 430–490 nm range. In the ESA region, τ_3 is below 20 ps for λ > 600 nm and rises slightly but significantly for shorter wavelengths, up to 24 ± 1 ps for 505–520 nm. This is consistent with the different long-time slopes of the 519 and 630 nm traces in Fig. 6.

The above spectral shifts occur on the time scale of τ_2, which follows a similar trend, *i.e.* increasing up to 6–8 ps in the 520 nm region. The present situation of excited state kinetics with spectral shifts is similar to our recent report on bidentate Fe(II) complexes, and poses the question whether τ_2 and τ_3 represent the decays, *i.e.* internal conversion into S_0, of two separate excited state populations. For **C1**, we rather opt for a sequential scenario, as for **C2** and **C4**, and assign the small amplitude τ_2 to a slow excited state relaxation for two main reasons. Firstly, τ_2 is an ESA decay time for >530 nm and an ESA rise time for 500–530 nm (Fig. 6 and 7). There, its amplitude is too large compared with what it would be for a GSB recovery (Fig. 7, bottom panel). In the minor ESA band (400–430 nm), τ_2 appears to be a rise time (*cf.* 420 nm trace in Fig. 6), even though the fit gives a small positive amplitude due to the high noise level (see Fig. SI29† for a better illustration of the rising ESA in the 490–510 nm and around 400–420 nm range). Second, comparing **C1** and **C2**, one can envisage that the lateral hexyl/methyl chains have an influence on details of the excited state structure suggesting an effect in the structural dynamics, thus modulating the energies of ESA transitions and the value and amplitude of τ_2 in a sequential reaction scenario. On the contrary, we do not expect the hexyl/methyl substitution to open a second faster excited state decay channel (τ_2 in addition to τ_3), which would lead to the "parallel" excited state relaxation scenario observed for bidentate complexes.[18] Therefore, **C1** obeys the same excited state relaxation scheme (1) as **C2** and **C4**. For **C3**, it is likely that τ_2 is also associated with IC into S_0 since this component appears as a recovery time throughout the GSB band (*cf.* Fig. SI33†). We will address the origin of the different lifetimes and the visibility of the τ_2-related structural relaxation process in the discussion section.

Computational analysis of the excited-state decay

The photophysics of the new dyes have been analysed by means of density functional theory (DFT) and its time-dependent DFT (TD-DFT) extension, given its proven good description of the electronic structure and the excited-state decay of related Fe(II) complexes.[13] Fig. 10 shows the calculated PESs for the lowest-lying triplet ^{3}MLCT and ^{3}MC states and the quintet ^{5}MC state for compounds **C1**, **C3** and **C4**. Note that the electronic structures of **C1** and **C2** are very similar since they only differ in the length of the alkyl chain, therefore only the **C1** complex has been modelled. Previous works on bidentate Fe-NHC systems reported that Fe–N or Fe–C bond elongations actually drive the excited-state decay also allowing singlet–triplet crossings with the ground state.[13,18,26] Thus, the curves have been built by means of relaxed scan calculations along one of the Fe–N bonds in order to explore the role of this coordinate in the excited-state decay in tridentate Fe(II) complexes. Note that such an approach while it has the advantage of a reduced computational cost compared to the full characterization of the PES by the calculation of minimum energy paths (MEP) only provides upper bounds to the energetic barriers encountered during the path.

It can be readily seen that the ^{3}MLCT minima are close to the Franck–Condon region, whereas the lowest point in the ^{3}MC curves is placed at larger Fe–N distances due to its inherent Fe–N antibonding character. It shall be noted that the adiabatic energy difference between the ^{3}MLCT and ^{3}MC lowest energy points in the PESs, for instance of **C4** (0.19 eV, see Fig. 10c), is in excellent agreement with the 0.12 eV value reported for a related compound with similar excited-state lifetime.[15]

Results displayed in Fig. 8 clearly indicate that the Fe–N stretching mediates the photoresponse also in tridentate Fe-NHC complexes, giving access to the ^{3}MC/S_0 intersystem crossings. Striking differences are however found between tridentate and bidentate complexes.[17] The ps range excited-state lifetime in the former can be explained by the exploration of planar or quasi planar triplet PES regions where S_0 lies above the triplet state manifold, acting as energy traps (spin crossover).[18] In tridentate compounds, the Fe–N bond stretch clearly destabilizes both S_0 and the triplet states, even though the destabilization is not uniform between the two states, hence allowing their crossing. The reason for the extended excited-state lifetime beyond the ultrafast sub-picosecond

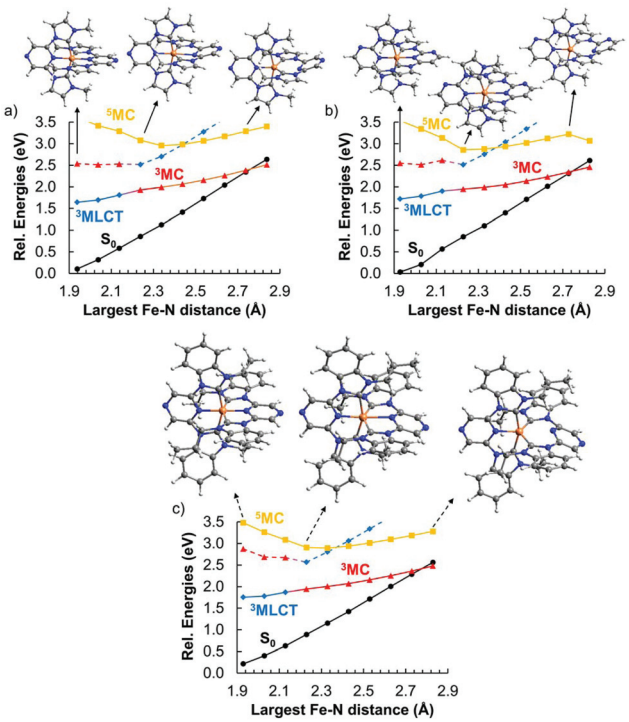

Fig. 8 Fe–N relaxed scan energy profiles of (a) **C1**, (b) **C3** and (c) **C4**. For the sake of simplicity, only the lowest-lying ^{3}MLCT, ^{3}MC and ^{5}MC states are shown.

regime can hence now be ascribed to the presence of energy barriers, found on the triplet PESs, connecting the Franck–Condon and the singlet–triplet crossing region. Note however, that the values of ~0.5 eV found for the barriers from the ^{3}MC minima to the corresponding ^{3}MC/S_0 singlet–triplet crossing points represent upper bounds and could be significantly lowered by the explicit calculations of the minimum energy paths. Furthermore, the non-adiabatic ^{3}MC → S_0 intersystem crossings could take place at regions with triplet-singlet energy differences of ~0.1–0.2 eV, and not necessarily at the crossing points shown in Fig. 8 (~2.73–2.74 Å). As a matter of fact, we have considered **C1** as a representative example to compute the T_1/S_0 spin–orbit coupling (SOC) along the PESs shown in Fig. 8a. The values at each Fe–N distance are shown in Table 3, indicating a strong coupling already at ~2.5–2.6 Å distances, supporting intersystem crossing events at shorter iron-nitrogen elongation and hence with a lower energy cost. The adiabatic evolution of T_1 from ^{3}MLCT to ^{3}MC at Fe–N distances of *ca.* 2.3 Å is also evidenced by the sudden increase in the SOC value of about 100 cm^{-1} between the 2.238 and 2.338 Å Fe–N distances.

Regarding the role of the lowest-lying quintet ^{5}MC state, the energy levels shown in Fig. 8 suggest a minor participation of this state in the excited-state decay since no ^{5}MC/S_0 crossings are predicted along the explored Fe–N distances. This consideration is coherent with the behaviour observed in bidentate Fe-NHC.[17,18]

Fig. 9 shows the adiabatic profile of the lowest-lying 20 triplet states for the pyrazine-based complexes **C1** and **C4**. As in the case of Fe-NHC bidentate complexes,[17] only the three lowest-energy triplet states lead to singlet–triplet crossing points, whereas the higher states are extremely destabilized by the Fe–N stretching. These results reveal the crucial role of these low-energy triplet states, since after light absorption an initial ultrafast intersystem crossing followed by vibrational cooling of the hot MLCT states is observed (see above). The upper bounds for the triplet energy barriers found in the present TD-DFT calculations (<0.5 eV for the Fe–N distances from ~2.2 to ~2.5–2.7 Å, see Fig. 8) are in agreement with the experimental estimations based on the Arrhenius equation (~0.1 eV), as depicted in the discussion section.

Table 3 T_1/S_0 SOCs for the **C1** complex

Fe–N (Å)	2.138	2.238	2.338	2.438	2.538	2.638
SOC (cm^{-1})	47	88	189	228	247	259

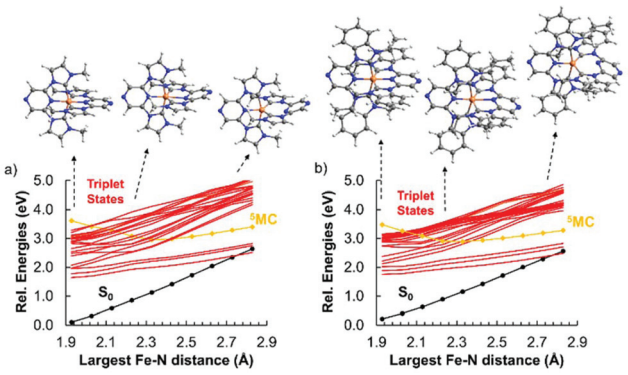

Fig. 9 Fe–N relaxed scan energy profiles of (a) **C1** and **C4**. The first 20 triplet states and the lowest-lying ^{5}MC states are shown.

Discussion

The four new compounds **C1–C4** investigated in this work extend our previous sets of Fe(II) complexes with bidentate and tridentate ligands bearing respectively three and four carbene bonds. In all cases, the ligand field enhancement is large enough to prevent excited state relaxation into the $^5T_2$ high spin manifold.[13] According to reaction scheme (1), ultrafast spectroscopy monitors the sub-100 fs ^{1}MLCT → ^{3}MLCT intersystem crossing, and, most importantly, the effect of the ligand's nature on the ^{3}MLCT/^{3}MC lifetime. The present combined experimental and theoretical study rationalises the combined effect of the electronic deficiency of the pyrazine and benzimidazolylidene (BIm) moieties in lowering the ^{3}MLCT energy, in analogy to the strategy described previously.[15]

We find that BIm is again most effective in this respect allowing to achieve, for **C4**, an excited state lifetime of τ_3 = 32 ± 2 ps, meaning a ≈30% increase with respect to **C1** and **C2**. As indicated in Fig. 8 and 9, the ISC and relaxation into the singlet ground state involves Fe–N stretching and thus a MLCT → MC conversion, but at the cost of an activation energy <0.5 eV according to the PESs. Alternatively, if we express τ_3 by the Arrhenius law, $\tau_3 = {\nu_0}^{-1} \exp(\Delta E/k_B T)$, and supposing ν_0 = 3–4 ps^{-1} for the excited state Fe–N stretch frequency, one may estimate the excited state barrier ΔE to be in the range of 3.5 to 5.0$k_B T$, meaning 90 to 130 meV (Fig. 10), in agreement with the TD-DFT computations. Slight modulations of the excited state energy landscape lead to the variation of a factor of ≈2.7 in the excited-state lifetime (12 to 32 ps).

A tentative explanation for the different excited-state lifetimes measured for the **C1–C4** series can be formulated on the basis of possible puckering motion in the ^{3}MLCT state, not considered in the present computations. In the ^{3}MLCT state, the extra charge on the diazine ring breaks the aromaticity, since the number of π electrons is now $4n + 3$, which can lead to out-of-plane (puckering) deformation, especially on the nitrogen coordinating the iron centre. The higher the electron density over the latter nitrogen atom, the larger the out-of-plane amplitude and thus the driving force for increasing the Fe–N distance. Comparing pyrazine-based complexes (**C1** and **C2**) and pyrimidine-based one (**C3**), that will have an asymmetric excited state charge distribution, one may expect, for the latter, a higher electron density on the Fe-coordinating nitrogen and thus a lower ΔE, consistent with the shorter excited-state lifetime observed. **C4**, on the other hand, will have a smaller excess electron density on the pyrazine ring

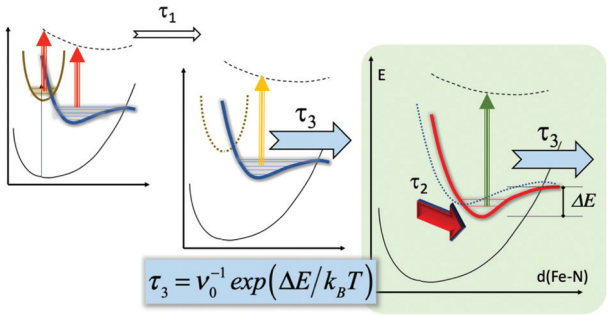

Fig. 10 Sketch of the ultrafast excited state relaxation processes, along the PES of ^{1}MLCT (brown) and the triplet manifold (blue/red). In phase 1, vibrational relaxation brings the population into the ^{3}MLCT state (τ_1). Structural and/or dielectric relaxation (red arrow) acts during phase 2, τ_2, and stabilises the populations in the red PES, leading to blue-shift of ESA. Population decay into S_0 takes place during both phases at the cost of a small activation barrier ΔE, situated along the Fe–N coordinate. Red, yellow and green arrows indicate the dynamically shifting ESA transitions.

since the BIm moieties have a larger electron accepting character.[15] The ring puckering driving force is thus minimal for **C4**, consistent with its longer excited-state lifetime. Further calculations are required to validate these hypotheses.

In addition to the excited-state lifetime, we report above a hitherto overlooked excited state relaxation process acting during τ_2. The effect manifested by the ESA blue-shift is most pronounced in **C1** and **C3**, while virtually absent in **C2** and **C4**. The latter are bearing lateral hexyl chains instead of methyl groups in the former. The long hexyl chains can interact with the diazine rings of the other tridentate ligand. We argue that this interaction hinders the above puckering motion, and thus the additional structural relaxation. Consequently, and since out-of-plane deformation increases the Fe–N and thus helps reaching the T_1/S_0 crossing points (see Fig. 10), the general trend of "more pronounced spectral relaxation effects go along with shorter excited state lifetimes" (**C1** and **C3**) is expected. An alternative explanation for the τ_2 process would refer to dynamic solvation, *i.e.* re-orientation of the polar acetonitrile solvent molecules as a response to the electron density increase on the ligands in the ^{3}MLCT states.[27] Here again, the hexyl chains would decrease the effect due to a reduced ligand–solvent interaction.

Conclusions

The present combined experimental and computational study investigates the effect of replacing pyridine by diazines in tridentate C^N^C heterocyclic ligands in Fe(II) complexes. It reveals several factors, which are beneficial in stabilising the excited-state, leading to an improved >30 ps excited-state lifetime for this class of four-carbene coordinating ligands. These ligands, as much as carboxylic acid groups used in our previous studies,[21] lower the MLCT energies in the Franck–Condon region, in addition to the BIm moieties. In addition, the present study confirms, from a computational viewpoint, the role of the Fe–N distance increase required for the excited state decay. Experiments indicated that an energy barrier must be overcome to reach the corresponding ^{3}MC/S_0 crossing points, which mediate the decay to the ground state. The possible role of the electronic charge distribution over the C^N^C ligands and the propensity of the diazine ring to undergo puckering motion is also discussed. The present work provides useful synthetic tools to design Fe(II) complexes with long-lived excited-state lifetimes, and represents a step further in the comprehension of the intricate photo processes taking place in first-row transition metal complexes.

Experimental and computational details

Synthesis

Solvents and commercially available reagents were used as received. Thin layer chromatography (TLC) was performed by using silica gel 60 F-254 (Merck) plates and visualized under UV light. Chromatographic purification was performed by using silica gel 60 (0.063–0.2 mm/70–230 mesh). ^{1}H (400 MHz) and ^{13}C NMR (100 MHz) spectra were taken on a DRX400 Bruker spectrometer at ambient temperature. The chemical shifts (δ), were calibrated by using either tetramethylsilane (TMS) or signals from the residual protons of the deuterated solvents and are reported in parts per million (ppm) from low to high field. High-resolution mass spectrometry (HRMS) data was obtained by using Bruker micrOTOF-Q spectrometer. UV-vis spectra were recorded in a 1 cm path length quartz cell on a LAMBDA 1050 (PerkinElmer), spectrophotometer. Cyclic voltammetry was performed on a Radiometer PST006 potentiostat using a conventional three-electrode cell. The saturated calomel electrode (SCE) was separated from the test compartment using a bridge tube. The solutions of studied complexes (0.2 mM) were purged with argon before each measurement. The test solution was acetonitrile containing 0.1 M Bu_4NPF_6 as supporting electrolyte. The working electrode was a vitreous carbon rod (1 cm^2) wire and the counter-electrode was a 1 cm^2 Pt disc. After the measurement, ferrocene was added as the internal reference for calibration. All potentials were quoted *versus* SCE. In these conditions the redox potential of the couple Fc^+/Fc was found at 0.39 V. In all the experiments the scan rate was 100 mV s^{-1}.

Synthesis of ligands

L1:[28] To a solution of 2,6-dichloropyrazine (300 mg, 2.01 mmol) in 40 mL of dioxane, was added an excess of 1-methyl-1*H*-imidazole (0.64 mL, 8.06 mmol) and the mixture was refluxed overnight. After cooling at room temperature, a saturated solution of KPF_6 was added (20 mL), the precipitate was washed with distilled water and dried under vacuum affording **L1** (750 mg, 70%). ^{1}H NMR (400 MHz, CD_3CN): δ 9.44 (s, 2H), 9.22 (s, 2H), 8.22 (s, 2H), 7.67 (s, 2H), 4.03 (s, 6H). ^{13}C NMR (101 MHz, CD_3CN): δ 141.6, 137.2, 136.3, 126.2,

120.1, 37.5. HRMS (ESI) calcd for $C_{12}H_{14}N_6P_2F_{12}$ m/z = 121.0634 $[M - 2PF_6]^{2+}$. Found: 121.0631.

L2: To a solution of 2,6-dichloropyrazine (180 mg, 1.21 mmol) in 20 mL of dioxane, was added an excess of 1-hexyl-1*H*-imidazole (736 mg, 4.83 mmol) and the mixture was refluxed overnight. After cooling at room temperature, a saturated solution of KPF_6 was added (10 ml), the precipitate was washed with distilled water and dried under vacuum affording **L2** (600 mg, 74%): ^{1}H NMR (400 MHz, CD_3CN) δ 9.48 (s, 2H), 9.23 (s, 2H), 8.26 (t, J = 1.9 Hz, 2H), 7.72 (t, J = 1.9 Hz, 2H), 4.33 (t, J = 7.4 Hz, 4H), 2.02–1.95 (m, 4H), 1.45–1.29 (m, 12H), 0.91 (t, J = 7.1 Hz, 6H). ^{13}C NMR (101 MHz, CD_3CN) δ 141.6, 137.1, 135.6, 124.9, 120.3, 51.4, 31.3, 29.8, 25.9, 22.7, 13.8. HRMS (ESI) calcd for $C_{22}H_{34}N_6PF_6$ m/z = 381.2761 $[M - PF_6]^+$. Found: 381.2765.

L3: To a solution of 2,4-dichloropyrimidine (250 mg, 1.68 mmol) in 30 mL of dioxane, was added an excess of 1-methyl-1*H*-imidazole (530 mg, 6.71 mmol) and the mixture was refluxed overnight. After cooling at room temperature, 40 mL of diethyl ether was added and the precipitate was filtered and dried under vacuum affording **L3** (405 mg, 77%): ^{1}H NMR (400 MHz, CD_3CN) δ 9.58 (s, 2H), 9.18 (d, J = 5.6 Hz, 1H), 8.30 (d, J = 17.1 Hz, 2H), 7.91 (d, J = 5.5 Hz, 1H), 7.64 (d, J = 8.7 Hz, 2H), 4.03 (s, 6H). ^{13}C NMR (101 MHz, D_2O) δ 163.9, 154.8, 152.3, 125.6, 125.0, 119.4, 110.6, 36.7. HRMS (ESI) calcd for $C_{12}H_{14}N_6Cl_2$ m/z = 121.0634 $[M - 2Cl]^{2+}$. Found: 121.0632.

L4:[28] A solution of benzimidazole (642 mg, 5.44 mmol) in anhydrous DMF (3 mL) was added dropwise to the suspension of NaH 95% (137 mg) in anhydrous DMF (3 mL) over a period of 15 min at room temperature under inert atmosphere. Then a solution of 2,6-dichloropyrazine (300 mg, 2.01 mmol) in anhydrous DMF (3 mL) was added, and the mixture was refluxed overnight. The reaction mass pH was then adjusted to pH 6.2 by adding 20 mL of distilled water. The precipitate formed was subsequently filtered and washed with water and dried under vacuum affording 2,6-bis(1*H*-benzo[*d*]imidazol-1-yl)pyrazine (BisBIm-Pz) (533 mg, 84%) ^{1}H NMR (400 MHz, DMSO-d_6) δ 9.32 (s, 2H), 9.19 (s, 2H), 8.29 (dd, J = 6.2, 2.6 Hz, 2H), 7.86 (dd, J = 6.2, 2.8 Hz, 2H), 7.49–7.34 (m, 4H). HRMS (ESI) calcd for $C_{20}H_{17}N_6$ m/z = 313.1196 $[M + H]^+$. Found: 341.1509. To a solution of BisBIm-Pz (150 mg, 0.48 mmol) in 2 mL DMF was added 0.18 mL of methyl iodide (1.93 mmol) and the mixture was refluxed overnight. After cooling at room temperature, a saturated solution of KPF_6 was added (10 ml), the precipitate was washed with distilled water and dried under vacuum affording **L4** (255 mg, 84%) ^{1}H NMR (400 MHz, DMSO-d_6) δ 10.77 (s, 2H), 9.61 (s, 2H), 8.45 (d, J = 8.2 Hz, 2H), 8.24 (d, J = 8.1 Hz, 2H), 7.83 (dt, J = 24.0, 7.7 Hz, 4H), 4.31 (s, 6H). ^{13}C NMR (101 MHz, DMSO-d_6) δ 144.0, 142.6, 139.1, 132.6, 129.7, 128.7, 128.1, 115.8, 114.9, 34.7. HRMS (ESI) calcd for $C_{12}H_{14}N_6I$ m/z = 341.1507 $[M - I]^+$. Found: 341.1509.

L5·Br: To a solution of BisBIm-Pz (150 mg, 0.78 mmol) in 3 mL DMF was added 0.46 mL 1-bromohexane (1.93 mmol) and the mixture was refluxed overnight. After cooling at room temperature, 30 mL diethyl ether was added and the precipitate was filtered and dried under vacuum affording **L5·Br** (225 mg, 73%) ^{1}H NMR (400 MHz, DMSO-d_6) δ 10.80 (s, 2H), 9.62 (s, 2H), 8.45 (d, J = 8.3 Hz, 2H), 8.32 (d, J = 8.2 Hz, 2H), 7.81 (dt, J = 15.3, 7.4 Hz, 4H), 4.70 (t, J = 7.3 Hz, 4H), 2.14–1.98 (m, 4H), 1.53–1.43 (m, 4H), 1.41–1.26 (m, 8H), 0.89 (t, J = 7.0 Hz, 6H). ^{13}C NMR (101 MHz, DMSO-d_6) δ 142.9, 142.0, 138.6, 131.4, 129.4, 128.1, 127.6, 115.5, 114.4, 47.5, 30.6, 28.3, 25.3, 21.8, 13.8. HRMS (ESI) calcd for $C_{30}H_{37}N_6Br_2$ m/z = 481.3074 $[M - 2Br]^+$. Found: 481.3044.

Synthesis of complexes

General procedure of the synthesis of **C1**, **C2** and **C3**: To a solution of the appropriate ligand L (1 eq.) in 2 mL of anhydrous DMF were added simultaneously a solution of KHMDS (4 eq.) in 2 mL anhydrous DMF and a solution of $FeBr_2$ (0.5 eq.) in anhydrous 1 mL DMF, the resulting dark red mixture was stirred at room temperature for 10 min. A saturated solution of KPF_6 was added (10 ml), and the precipitate was collected by filtration. The solid was purified by column chromatography eluting with an acetone/H_2O/KNO_3 (sat) = 10 : 3 : 1 mixture. The yellow fraction was collected and after the evaporation of acetone, the left solution was treated with a saturated solution of KPF_6. Affording the precipitation of the complex, it was then filtered, washed with distilled water and dried under vacuum.

C1: The general procedure starting from **L1** (148 mg, 0.28 mmol), KHMDS (222 mg, 1.11 mmol) and $FeBr_2$ (30 mg, 0.14 mmol) gave **C1** (23 mg, 20% yield). ^{1}H NMR (400 MHz, CD_3CN) δ 9.04 (s, 4H), 8.13 (d, J = 2.2 Hz, 4H), 7.04 (d, J = 2.2 Hz, 4H), 2.51 (s, 12H).^{13}C NMR (101 MHz, CD_3CN) δ 198.0, 150.9, 128.0, 126.6, 117.5, 35.2. HRMS (ESI) calcd for $C_{24}H_{24}FeN_{12}P_2F_{12}$ m/z = 268.0793 $[M - 2PF_6]^{2+}$. Found: 268.0816.

C2: The general procedure starting from **L2** (187 mg, 0.28 mmol), KHMDS (222 mg, 1.11 mmol) and $FeBr_2$ (46 mg, 0.14 mmol) gave **C2** (23 mg, 30% yield). ^{1}H NMR (400 MHz, CD_3CN): δ 9.12 (s, 4H), 8.23 (d, J = 2.2 Hz, 4H), 7.18 (d, J = 2.3 Hz, 4H), 2.60 (t, J = 2.2 Hz 8H), 1.17–1.09 (m, 8H), 1.04–0.95 (m, 8H), 0.82 (t, J = 7.3 Hz, 20H), 0.66–0.56 (m, 8H).^{13}C NMR (101 MHz, CD_3CN) δ 196.6, 150.9, 127.1, 126.7, 49.7, 31.6, 31.0, 26.2, 22.7, 13.8. HRMS (ESI) calcd for $C_{44}H_{64}N_{12}P_2F_{12}$ m/z = 408.2358 $[M - 2PF_6]^{2+}$. Found: 408.2406.

C3: The general procedure starting from **L3** (101 mg, 0.32 mmol), KHMDS (238 mg, 1.30 mmol) and $FeBr_2$ (35 mg, 0.16 mmol) gave **C3** (20 mg, 15% yield). ^{1}H NMR (400 MHz, CD_3CN): δ 8.91 (d, J = 5.6 Hz, 2H), 8.08 (dd, J = 15.1, 2.1, 4H), 7.79 (d, J = 5.7 Hz, 2H), 7.06 (dd, J = 9.7, 2.0 Hz, 4H), 2.56 (d, J = 5.5 Hz, 12H).^{13}C NMR (101 MHz, CD_3CN) δ 202.1, 199.4, 161.2, 159.4, 157.2, 128.4, 127.8, 116.8, 102.9, 35.5, 35.51. HRMS (ESI) calcd for $C_{24}H_{24}FeN_{12}P_2F_{12}$ m/z = 268.0793 $[M - 2PF_6]^{2+}$. Found: 268.0811.

C4: A Schlenk tube was loaded with **L5·Br** (149 mg, 0.23 mmol) then 5 mL of dry THF was added under inert atmosphere. The reaction mixture was cooled to −10 °C and LiHMDS (0.46 mL, 0.46 mmol, 1 M in THF) was added dropwise over 30 min. The cooling bath was removed, and the temperature allowed to raise slowly up to 20 °C. The reaction mixture was then stirred for 1 h. A solution of anhydrous $FeBr_2$

(25 mg, 0.11 mmol) in dry THF (3 mL) was finally added *via* syringe to the Schlenk tube. The reaction mixture was stirred at room temperature for 24 h after which, the solvent was removed under reduced pressure. 3 mL of distilled water was added followed by 10 mL of a saturated solution of KPF_6 and the precipitate was collected by filtration. The solid was purified by column chromatography eluting with a acetone/H_2O/KNO_3 (sat.) = 10 : 3 : 1 mixture. The yellow fraction was collected and after the evaporation of acetone, the residue was treated with a saturated solution of KPF_6 leading to precipitation of the complex that was then filtered, washed with distilled water and dried under vacuum giving **C4** (20 mg, 13% yield). ^{1}H NMR (400 MHz, DMSO-d_6): δ 9.51 (s, 4H), 8.13 (d, J = 8.4 Hz, 4H), 7.98 (d, J = 8.3 Hz, 4H), 7.48 (dt, J = 15.4, 7.5 Hz 8H), 2.80 (t, J = 8.1, 8H). 1.21–1.10 (m, 8H), 1.06–0.97 (m, 8H), 0.98–0.82 (m, 20H), 0.64 (t, J = 7.1, 8H).^{13}C NMR (101 MHz, DMSO-d_6) δ 193.1, 140.5, 137.1, 129.9, 127.9, 126.6, 126.0, 113.9, 112.8, 49.8, 31.7, 31.1, 26.3, 22.8, 13.9. HRMS (ESI) calcd for $C_{60}H_{72}FeN_{12}P_2F_{12}$ m/z = 508.2671 $[M - 2PF_6]^{2+}$. Found: 508.2656.

Computational details

The ground-state equilibrium structures of all the complexes have been optimized using the standard DFT/B3LYP functional in combination with the 6-31+G(d,p), as implemented in the Gaussian 09 (D.01 revision) software package.[29] This computational protocol has repeatedly proven its ability to describe the Franck–Condon geometry of many Fe(II) complexes.[30–32] Note that the hexyl groups of **C4** have been substituted by ethyl groups in order to make the computations more affordable. The excited states at the Franck–Condon area have been computed by means of the TD-DFT method using the Tamm–Dancoff approximation,[33] in particular making use of the exchange correlation functional HCTH407 (hereafter, TD-HCTH),[34] according to previous studies on similar Fe-NHC systems as documented by our research group.[13,15,17,21,35] The theoretical spectra reported in the ESI† have been obtained by sampling the nuclear density of the Franck–Condon region through a semiclassical Wigner distribution of 20 structures, and convoluting the excitation energies with Gaussian functions with a full-width at half-length (FWHL) of 0.3 eV. The first 40 singlet–singlet vertical absorptions have been computed for each geometry, making use of the larger 6-311G(d,p) basis set.

The nature of the excitations have been determined by computing the NTOs,[36,37] *via* post-processing of their density matrices obtained with the TD-HCTH method, using the NANCY_EX code.[37,38] For the readers' convenience, we remind that NTOs may be considered as the best orbitals to describe a given electronic transition, and in contrast to the Kohn–Sham representation, often one or two couples of occupied/virtual orbitals are enough to fully describe the electronic density rearrangement in the excited state.

Whereas all triplet energies reported in the present work have been obtained with the TD-HCTH method and the 6-311G(d,p) basis set, different optimization techniques and basis sets have been employed to compute the different geometries that compose the PESs. The ^{3}MLCT equilibrium geometries have been obtained by means of TD-HCTH/6-31 + G(d,p) optimizations using standard minimization algorithms. Starting from the latter structures, the Fe–N connectivity with the largest bond distance have been elongated through relaxed scan calculations defining increments of 0.1 Å. The smaller 6-31G* basis set have been used to make the scan calculations affordable. The converged scan points show the absence of any relevant geometry with several Fe–N or Fe–C bonds enlarged simultaneously, since the relaxed scan algorithm freezes only one Fe–N bond whereas the rest is optimized without constraints. Final energies have been subsequently recomputed using the 6-311G(d,p) basis set, and the ^{3}MLCT or ^{3}MC nature of the state have been determined by computing the NTOs at each geometry. Note that the scan profiles estimate the presence of ^{3}MC minima, in agreement with related Fe(II) complexes.[13,39] Scan calculations using the unrestricted (u)-DFT method leads to extremely similar results as reported in the ESI (see Fig. S21†). On the other hand, the quintet ^{5}MC states have been calculated using the unrestricted DFT/HCTH ansatz.

The singlet–triplet SOCs $\psi_S|\hat{H}_{SO}|\psi_T$, where $\hat{H}_{SO}$ refers to the spin–orbit Hamiltonian, have been computed using the ADF 2018 modelling suite,[40–42] employing the TD-HCTH method and making use of the DZP basis set for all atoms except for iron, described with the TZP basis set.

Femtosecond transient absorption spectroscopy

The 800 nm output of a 5 kHz Ti:Sapphire amplifier (Amplitude Technologies) is sent into a commercial optical parametric amplifier (TOPAS, Light Conversion) to obtain the pump beam at 480 nm (pulse duration of ~60 fs). 0.4–0.5 mW average power (80–100 μJ per pulse) is used to work in a regime of linear signal response. In order to generate the broadband white-light, a small portion of the initial 800 nm beam is focused onto a CaF_2 crystal, mounted on a loudspeaker to prevent thermal degradation. The TA data and a reference beam are acquired in the range 350–680 nm using a Peltier-cooled charge-coupled device (CCD), which is operated at 220 Hz spectral read-out rate, and the exit of a 25 cm focal length spectrometer (resolution 3 nm). The polarization of pump and probe beams is set at the magic angle (54.7°) and both are focalised into the sample with a diameter of 60 and 40 μm respectively. The complexes are dissolved in AcN in a 1 mm quartz cell (O.D. ≈ 0.3). The transient absorption spectra of the complexes and the solvent are acquired. All of them are treated to correct for Group Velocity Dispersion (±50 fs). The solvent data are subtracted (corrected with an appropriate factor in order to remove the Raman signals of CH_3CN and the cross-phase modulation artefacts (see ref. 43). A detailed qualitative analysis of the spectra and the kinetics is performed. This is followed, when indicated, by Single Value Decomposition (SVD) and Global Analysis (using Glotaran, http://www.glotaran.org) for **C4** and **C2** while, for the others, single wavelength fits are made. In this case, a multi-exponen-

tial is convoluted by the temporal instrument response function (IRF), assumed to be a Gaussian, centred at t = ±50 fs, with 60 fs FWHM (see ESI†).

Conflicts of interest

There are no conflicts to declare.

Acknowledgements

The project is funded by the French Agence Nationale de Recherche (ANR-16-CE07-0013-02). The L2CM team is grateful to F. Lachaud for mass spectrometry. The Strasbourg team thanks O. Crégut, J. Brazard and J. Léonard for help and fruitful discussions. Molecular modelling has been performed on the LPCT local computing resources. A. F.-M. acknowledges the Région Grand Est government (France) and the ANR agency for postdoctoral contracts, and the MINECO project CTQ2017-87054-C2-2-P (Spain). The Strasbourg group acknowledges financial support through the Labex NIE. This article is a proof of the LPCT team's recognition of Jean-François Hallet's accomplishments in the field of theoretical studies of transition metal compounds.

References

1 W. R. Browne and B. L. Feringa, *Nat. Nanotechnol.*, 2006, **1**, 25–35.
2 J. Kalinowski, V. Fattori, M. Cocchi and J. A. G. Williams, *Coord. Chem. Rev.*, 2011, **255**, 2401–2425.
3 B. Colasson, A. Credi and G. Ragazzon, *Coord. Chem. Rev.*, 2016, **325**, 125–134.
4 E. Longhi and L. De Cola, in *Iridium(III) in Optoelectronic and Photonics Applications*, ed. E. Zysman-Colman, John Wiley & Sons, Ltd, Chichester, UK, 2017, pp. 205–274.
5 A. Hagfeldt, G. Boschloo, L. Sun, L. Kloo and H. Pettersson, *Chem. Rev.*, 2010, **110**, 6595–6663.
6 C. D. Clark, M. Z. Hoffman, D. Paul Rillema and Q. G. Mulazzani, *J. Photochem. Photobiol., A*, 1997, **110**, 285–290.
7 W. Gawelda, A. Cannizzo, V.-T. Pham, F. van Mourik, C. Bressler and M. Chergui, *J. Am. Chem. Soc.*, 2007, **129**, 8199–8206.
8 J. K. McCusker, K. N. Walda, R. C. Dunn, J. D. Simon, D. Magde and D. N. Hendrickson, *J. Am. Chem. Soc.*, 1993, **115**, 298–307.
9 J. E. Monat and J. K. McCusker, *J. Am. Chem. Soc.*, 2000, **122**, 4092–4097.
10 C. Consani, M. Prémont-Schwarz, A. ElNahhas, C. Bressler, F. van Mourik, A. Cannizzo and M. Chergui, *Angew. Chem., Int. Ed.*, 2009, **48**, 7184–7187.
11 O. S. Wenger, *J. Am. Chem. Soc.*, 2018, **140**, 13522–13533.
12 Y. Liu, P. Persson, V. Sundström and K. Wärnmark, *Acc. Chem. Res.*, 2016, **49**, 1477–1485.
13 T. Duchanois, L. Liu, M. Pastore, A. Monari, C. Cebrián, Y. Trolez, M. Darari, K. Magra, A. Francés-Monerris, E. Domenichini, M. Beley, X. Assfeld, S. Haacke and P. Gros, *Inorganics*, 2018, **6**, 63.
14 P. Chábera, K. S. Kjaer, O. Prakash, A. Honarfar, Y. Liu, L. A. Fredin, T. C. B. Harlang, S. Lidin, J. Uhlig, V. Sundström, R. Lomoth, P. Persson and K. Wärnmark, *J. Phys. Chem. Lett.*, 2018, **9**, 459–463.
15 L. Liu, T. Duchanois, T. Etienne, A. Monari, M. Beley, X. Assfeld, S. Haacke and P. C. Gros, *Phys. Chem. Chem. Phys.*, 2016, **18**, 12550–12556.
16 M. Pastore, T. Duchanois, L. Liu, A. Monari, X. Assfeld, S. Haacke and P. C. Gros, *Phys. Chem. Chem. Phys.*, 2016, **18**, 28069–28081.
17 A. Francés-Monerris, K. Magra, M. Darari, C. Cebrián, M. Beley, E. Domenichini, S. Haacke, M. Pastore, X. Assfeld, P. C. Gros and A. Monari, *Inorg. Chem.*, 2018, **57**, 10431–10441.
18 K. Magra, E. Domenichini, A. Francés-Monerris, C. Cebrián, M. Beley, M. Darari, M. Pastore, A. Monari, X. Assfeld, S. Haacke and P. C. Gros, *Inorg. Chem.*, 2019, **58**, 5069–5081.
19 R. E. Andrew, L. González-Sebastián and A. B. Chaplin, *Dalton Trans.*, 2016, **45**, 1299–1305.
20 A. A. Danopoulos, N. Tsoureas, J. A. Wright and M. E. Light, *Organometallics*, 2004, **23**, 166–168.
21 T. Duchanois, T. Etienne, C. Cebrián, L. Liu, A. Monari, M. Beley, X. Assfeld, S. Haacke and P. C. Gros, *Eur. J. Inorg. Chem.*, 2015, **2015**, 2469–2477.
22 R. L. Martin, *J. Chem. Phys.*, 2003, **118**, 4775–4777.
23 J. J. Snellenburg, S. P. Laptenok, R. Seger, K. M. Mullen and I. H. M. van Stokkum, *J. Stat. Softw.*, 2012, **49**(3), DOI: 10.18637/jss.v049.i03.
24 T. Duchanois, L. Liu, M. Pastore, A. Monari, C. Cebrián, Y. Trolez, M. Darari, K. Magra, A. Francés-Monerris, E. Domenichini, M. Beley, X. Assfeld, S. Haacke and P. Gros, *Inorganics*, 2018, **6**, 63–63.
25 Y. Liu, T. Harlang, S. E. Canton, P. Chábera, K. Suárez-Alcántara, A. Fleckhaus, D. A. Vithanage, E. Göransson, A. Corani, R. Lomoth, V. Sundström and K. Wärnmark, *Chem. Commun.*, 2013, **49**, 6412.
26 P. Chábera, K. S. Kjaer, O. Prakash, A. Honarfar, Y. Liu, L. A. Fredin, T. C. B. Harlang, S. Lidin, J. Uhlig, V. Sundström, R. Lomoth, P. Persson and K. Wärnmark, *J. Phys. Chem. Lett.*, 2018, **9**, 459–463.
27 A. Rondi, Y. Rodriguez, T. Feurer and A. Cannizzo, *Acc. Chem. Res.*, 2015, **48**, 1432–1440.
28 G. Roymahapatra, S. Giri, A. A. Danopoulos, P. K. Chattaraj, A. Mahapatra, V. Bertolasi and J. Dinda, *Inorg. Chim. Acta*, 2012, **383**, 83–90.
29 M. J. Frisch, G. W. Trucks, H. B. Schlegel, G. E. Scuseria, M. A. Robb, J. R. Cheeseman, G. Scalmani, V. Barone, B. Mennucci, G. A. Petersson, H. Nakatsuji, M. Caricato, X. Li, H. P. Hratchian, A. F. Izmaylov, J. Bloino, G. Zheng, J. L. Sonnenberg, M. Hada, M. Ehara, K. Toyota, R. Fukuda,

J. Hasegawa, M. Ishida, T. Nakajima, Y. Honda, O. Kitao, H. Nakai, T. Vreven, J. A. Montgomery Jr., J. E. Peralta, F. Ogliaro, M. Bearpark, J. J. Heyd, E. Brothers, K. N. Kudin, V. N. Staroverov, R. Kobayashi, J. Normand, K. Raghavachari, A. Rendell, J. C. Burant, S. S. Iyengar, J. Tomasi, M. Cossi, N. Rega, J. M. Millam, M. Klene, J. E. Knox, J. B. Cross, V. Bakken, C. Adamo, J. Jaramillo, R. Gomperts, R. E. Stratmann, O. Yazyev, A. J. Austin, R. Cammi, C. Pomelli, J. W. Ochterski, R. L. Martin, K. Morokuma, V. G. Zakrzewski, G. A. Voth, P. Salvador, J. J. Dannenberg, S. Dapprich, A. D. Daniels, O. Farkas, J. B. Foresman, J. V. Ortiz, J. Cioslowski and D. J. Fox, *Revis. D01*, Gaussian Inc., Wallingford CT, 2010.

30 P. Verma, Z. Varga, J. E. M. N. Klein, C. J. Cramer, L. Que and D. G. Truhlar, *Phys. Chem. Chem. Phys.*, 2017, **19**, 13049–13069.

31 B. D. Alexander, T. J. Dines and R. W. Longhurst, *Chem. Phys.*, 2008, **352**, 19–27.

32 D. N. Bowman and E. Jakubikova, *Inorg. Chem.*, 2012, **51**, 6011–6019.

33 S. Hirata and M. Head-Gordon, *Chem. Phys. Lett.*, 1999, **314**, 291–299.

34 A. D. Boese and N. C. Handy, *J. Chem. Phys.*, 2001, **114**, 5497–5503.

35 T. Duchanois, T. Etienne, M. Beley, X. Assfeld, E. A. Perpète, A. Monari and P. C. Gros, *Eur. J. Inorg. Chem.*, 2014, **2014**, 3747–3753.

36 R. L. Martin, *J. Chem. Phys.*, 2003, **118**, 4775–4777.

37 T. Etienne, X. Assfeld and A. Monari, *J. Chem. Theory Comput.*, 2014, **10**, 3896–3905.

38 T. Etienne, X. Assfeld and A. Monari, *J. Chem. Theory Comput.*, 2014, **10**, 3906–3914.

39 A. Francés-Monerris, P. C. Gros, X. Assfeld, A. Monari and M. Pastore, *ChemPhotoChem*, DOI: 10.1002/cptc.201900100.

40 *ADF2018, SCM, Theoretical Chemistry*, Vrije Universiteit, Amsterdam, The Netherlands, https://www.scm.com.

41 C. Fonseca Guerra, J. G. Snijders, G. te Velde and E. J. Baerends, *Theor. Chem. Acc.*, 1998, **99**, 391–403.

42 G. te Velde, F. M. Bickelhaupt, E. J. Baerends, C. Fonseca Guerra, S. J. A. van Gisbergen, J. G. Snijders and T. Ziegler, *J. Comput. Chem.*, 2001, **22**, 931–967.

43 T. Roland, J. Léonard, G. Hernandez Ramirez, S. Méry, O. Yurchenko, S. Ludwigs and S. Haacke, *Phys. Chem. Chem. Phys.*, 2012, **14**, 273–279.